

Supporting Information for Temperature Gated Thermal Rectifier for Active Heat Flow Control

Jia Zhu¹[⊙], Kedar Hippalgaonkar¹[⊙], Sheng Shen¹, Kevin Wang², Yohannes Abate³,
Sangwook Lee², Junqiao Wu², Xiaobo Yin¹, Arun Majumdar¹[#], Xiang Zhang¹[#]

¹Department of Mechanical Engineering, University of California at Berkeley, Berkeley, CA 94720, USA.

²Department of Materials Science and Engineering, University of California at Berkeley, Berkeley, CA 94720, USA.

³Department of Physics and Astronomy, Georgia State University, Atlanta, GA 30303 USA

Corresponding Authors: E-mail: xiang@berkeley.edu and 4majumdar@gmail.com

Author Contributions: [⊙] These authors contributed equally

1. Methods

Synthesis of VO₂ beams

Bulk VO₂ powder was placed in a quartz boat in the center of a horizontal tube furnace. The typical growth temperature was 1000 °C with Ar used as the carrier gas. The VO₂ beams were collected on a Si substrate with a 500nm thick thermally grown surface oxide downstream from the source boat. The catalyst, which determines the size of the beam, can be partially diffused away by tuning the pressure and temperature to induce tapered or asymmetrical beam growth.

2. Thermal Conductance Measurement of Single VO₂ Beam

A resistive heater is used to heat the whole Si chip uniformly inside a cryostat to control the global device temperature, T_G . For thermal conductance measurements, a small DC

current ($\sim 6 \mu\text{A}$) is passed through the platinum (Pt) coil on one of the membranes to heat it to a temperature, T_h , above T_G , thus inducing a heat flow Q through the VO_2 beam to heat up the other membrane to T_s . An AC current of 500 nA is passed through the Pt coils on both membranes to determine its electrical resistance through a 4-point technique, which is then used to estimate the temperatures T_h and T_s . Using two SRS 850 lock-in amplifiers for the AC signals, signals from the sensing side were measured using a frequency of 199 Hz whereas that for the heating side utilized 1.11 kHz . Details of the experimental procedure can be found elsewhere ^{1,2}, while the error analysis from this experimental procedure is discussed later in the Supplementary Information. The resistance of the patterned coils, R_h and R_s varies between 3 and $5 \text{ k}\Omega$ at room temperature for different devices and is proportional to the temperature of the pads. Following the analysis of Shi et. al. ¹, the thermal conductance of the Platinum beams that suspended each platform can be described as follows:

$$G_l = \frac{P}{(\Delta T_h + \Delta T_s)} \quad (\text{SI } 1)$$

Here, a known power P was supplied to the Pt coil heater on one SiN_x membrane which also takes into account heat losses through the supporting legs, while resistance changes of the heater and sensor were used to determine the resulting temperature changes of the heater ($\Delta T_h = T_h - T_G$) and sensor ($\Delta T_s = T_s - T_G$) pads. Again following careful heat transfer analysis accounting for uniform joule heating in the Silicon Nitride (SiN_x) legs that suspended the platforms ^{1,2}, it can be shown that $P = I_h^2 (R_h + R_{leg})$. Here I_h is the DC current supplied, $R_h \sim 3 \text{ k}\Omega$ is the resistance of the Platinum coil on the heating side and $R_{leg} \sim 3 \text{ k}\Omega$ is the electrical resistance of one out of six SiN_x legs that help suspend each

platform. At 300K, we can estimate that the heat loss through the SiN_x legs using the equation (SI 1) is $G_l \sim 100 nW/K$.

For an actual thermal device where the heating current is 6 μA , $R_h = 3.336 k\Omega$, $R_l = 3.340 k\Omega$, with a VO₂ beam placed across the heating and sensing pads, we obtain $\Delta T_h = 2.49 K$ and $\Delta T_s = 0.96 K$, which results in a leg conductance of $G_l = 69.5 nW/K$.

Note here that using a 500 nA rms AC current on the heating and sensing pads to measure the resistances thus only gives a temperature rise on either membrane of $\Delta T_{h,AC} = \Delta T_{s,AC} \sim 10 mK$, which is below the temperature fluctuations in the cryostat and only causes an additional increase in temperature excursion of $\Delta T_{AC}/\Delta T_s \sim 10 mK/1K \sim 1\%$.

Further, the heat flow through the VO₂ beam, Q can be determined as a function of $\Delta T = T_h - T_s$, which is typically maintained close to 1K. The thermal conductance G of the VO₂ beams can hence be determined from ΔT_h and ΔT_s with the use of the relation

$$G = \frac{P}{\Delta T_h - \Delta T_s} \left(\frac{\Delta T_s}{\Delta T_h + \Delta T_s} \right) \quad (SI 2)$$

The DC power input, P is known to a very high accuracy (<0.5%), while the temperature measurement uses the temperature coefficient of resistivity (TCR) of the Platinum thin film on either membrane(<2%) (see below for error analysis). The thermal measurement technique only measures a two-probe conductance, which includes the thermal contact resistance between the beams and the membrane. The contact resistance is shown to be negligible and in the limiting case, contributing insignificantly to the rectification behaviour (see below for details).

3(a). Heat flow and heat flow deviation as a function of temperature difference across a uniform VO₂ beam at 300K and 360K

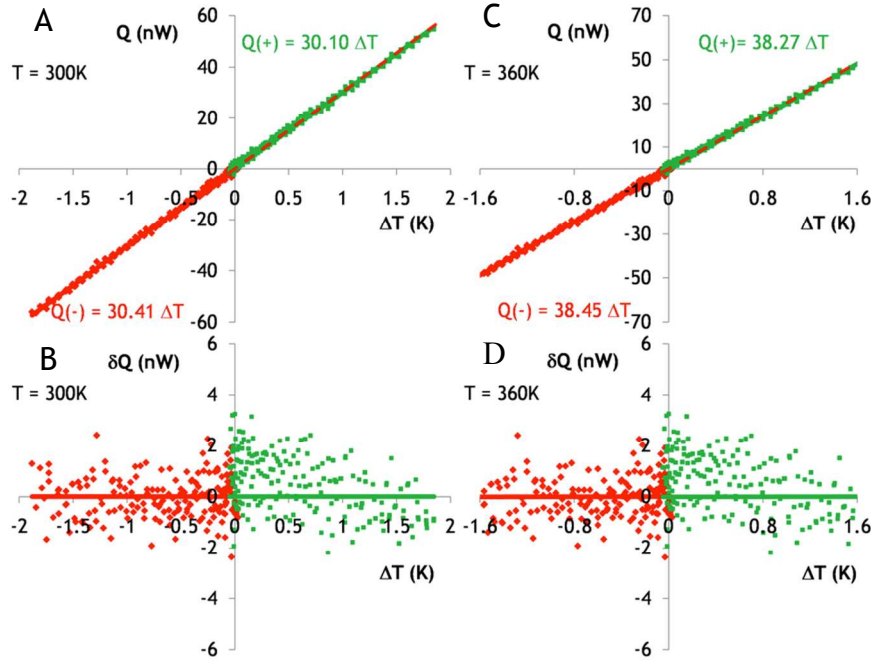


Fig. S1 A) and C) Heat flow (Q) as a function of temperature difference (ΔT) across the uniform VO₂ beams at 300K and 360K respectively. Different signs (+) and (-) of thermal power (Q) represent different directions of heat transfer. B) and D) Heat flow deviation (δQ) from linear fit as a function of temperature difference (ΔT) across the VO₂ beams at 300K and 360K correspondingly.

3(b). Temperature dependent conductance for a uniform VO₂ beam without rectification

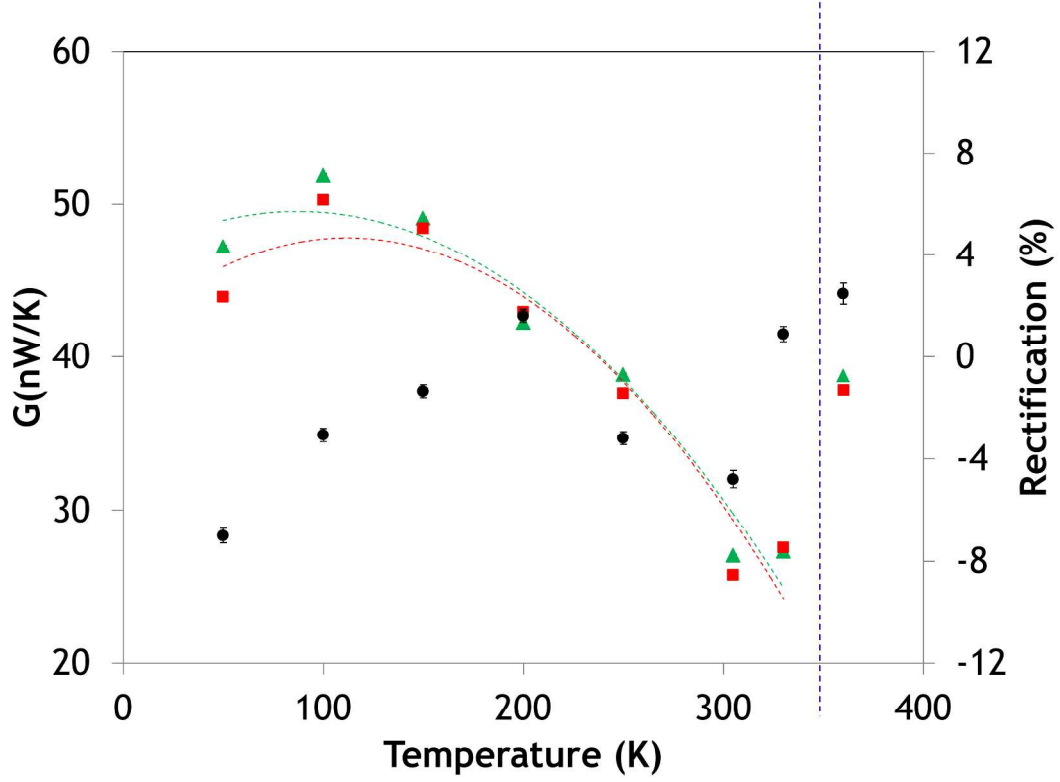


Fig. S2 Thermal conductance of a uniform VO₂ beam (the same as SI section 2(a)) along two opposite directions (green and red filled squares) as a function of global temperature. Also shown is the corresponding thermal rectification (black closed circles) that suggests no appreciable rectification. Note the phase transition temperature of 340K shown by a vertical blue dashed line.

4(a). Temperature dependent conductance for an asymmetrical VO₂ beam showing rectification – Beam II in main manuscript (Table I)

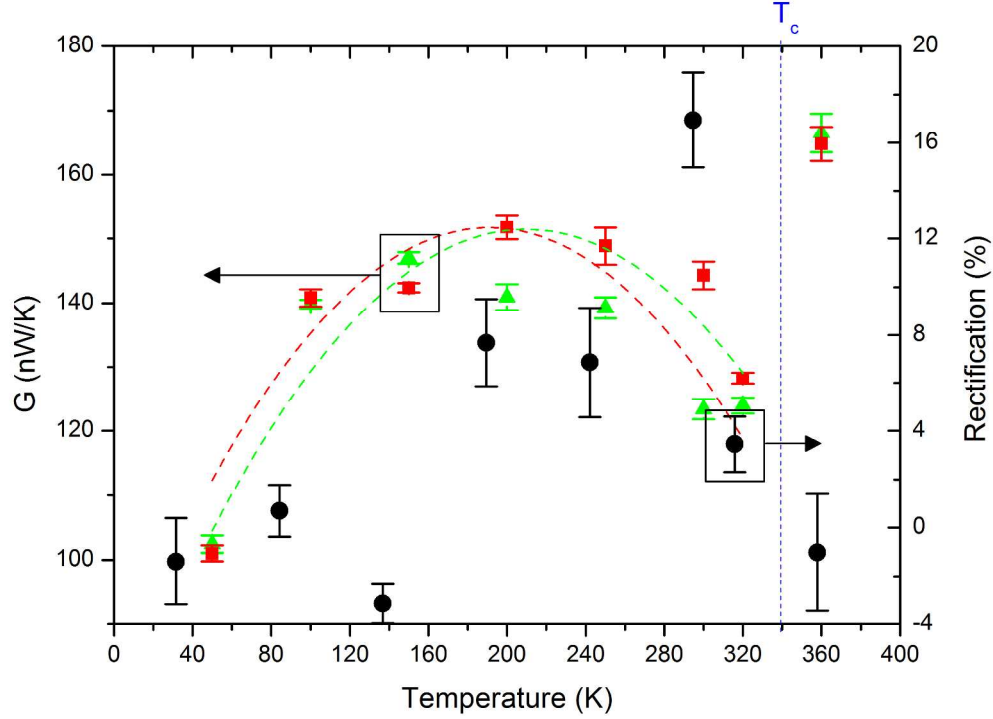
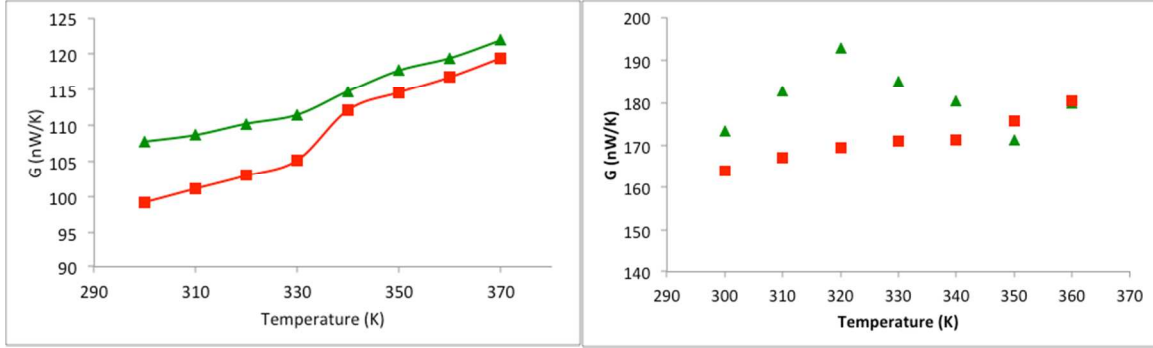


Fig. S3 Thermal conductance of the VO₂ beam II (see Table 1 in main manuscript) as a function of global heating temperature along two opposite directions, represented by two different symbols (green triangular and red squares). Also shown is the rectification (closed black circles) and its corresponding error bar. Thermal rectification ranges from 8 ± 1 % up to 16 ± 1.2 % in the temperature range from 200 to 340K.

4(b). Temperature dependent conductance for Beams III-VI in the main manuscript (Table I)

Beam III and IV:



Beam V and VI:

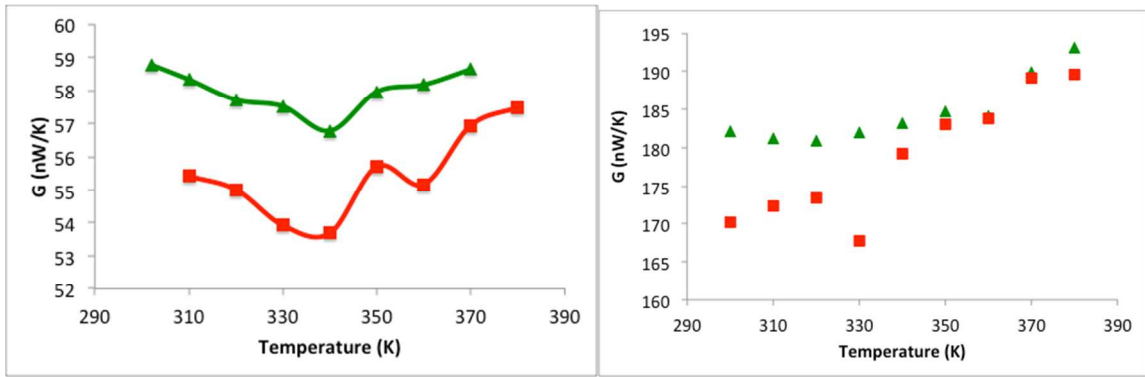


Fig. S4 Temperature Dependent Conductance of Beams III-VI in the main manuscript (Table I). Rectification in Beam V does not switch off in the purported fully-metallic phase. The temperature dependence of conductance is different for different beams and we hypothesize that this is due to the conflicting effect of phonon scattering and interfaces.

5. Electrical Measurement on VO₂ beams

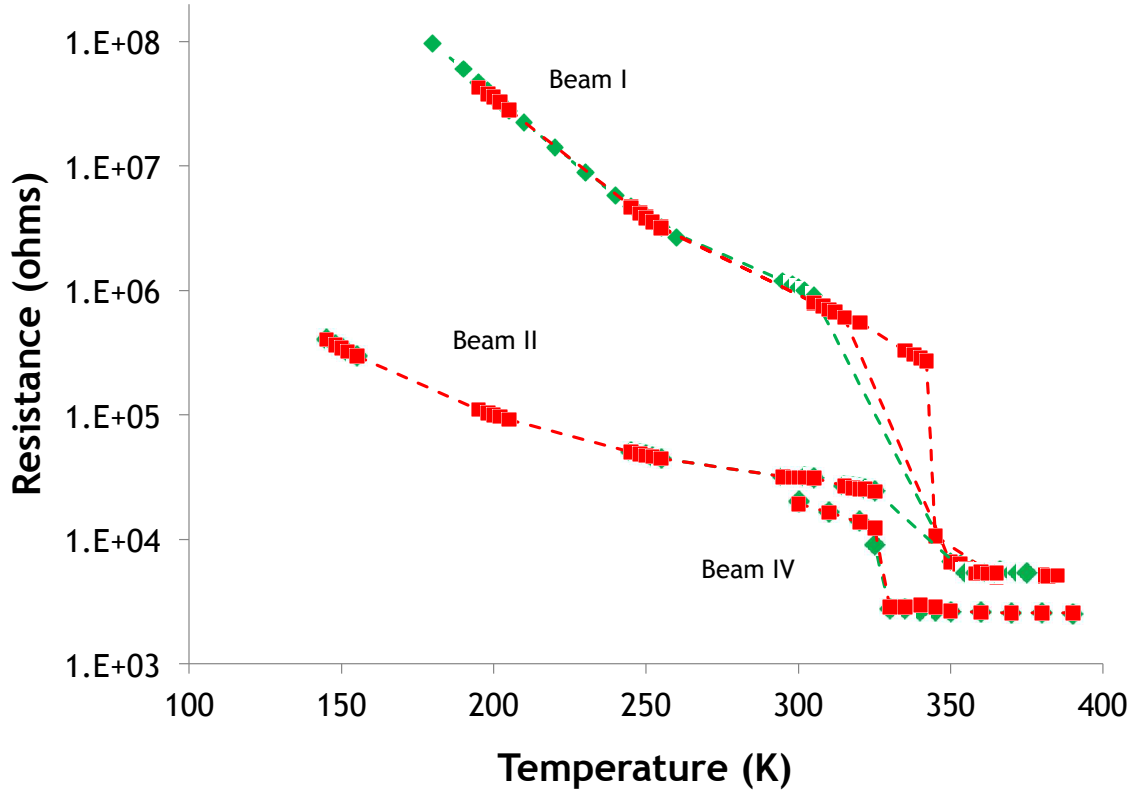


Fig. S5 Electrical resistance of three asymmetrical VO₂ beams as a function of global heating temperature, showing the electrical phase transition at 340K. It is a two probe measurement performed at the same temperature as the thermal conductance measurement. Except for the temperatures close to phase transition, the electrical rectification is below 1%.

6. Near-field Infrared Spectroscopic Study on VO₂ Beams

Near-field infrared spectroscopic imaging was performed with a (scattering type scanning near-field microscope (s-SNOM) which is based on a tapping mode AFM. Vertically vibrating PtIr-coated Si-tip (apex radius $R \approx 20$ nm) with an amplitude of about 25-30 nm at a frequency of $\Omega \approx 280$ kHz is illuminated by a focused CO₂ laser beam at wavelength, $\lambda=10.7$ μm . The tip converts the illuminating radiation diffraction limited spot into a highly localized and enhanced near field at the tip apex. Due to the near-field interaction between tip and sample, the back-scattered radiation from the probe tip is modified in both amplitude and phase, commensurate to the local dielectric response of the sample.^{3,4} The tip-scattered light is detected using a pseudo-heterodyne interferometric detection scheme, which enables simultaneous recording of amplitude and phase of the scattered field³⁻⁵. Background signals are efficiently suppressed by demodulating the detector signal at the second harmonic of the tip oscillating frequency.

The contrast formation in s-SNOM near-field imaging of metal-insulator transition (MIT) in VO₂ is understood by considering the scattered signal at the second harmonic of the tip frequency as a function of the optical constants of the tip and the sample. Metallic regions show higher scattering amplitude owing to large negative real part and large positive imaginary part of the optical constants at $\lambda=10.7$ μm . Insulating regions have lower scattering amplitudes because of the small imaginary and real part of the optical constants. This difference in locally varying optical constants, and thus s-SNOM scattering amplitude signal, provides the basis for image contrast formation of the metal and insulating phases in VO₂.

We directly observe the nanoscale spatial evolution of one phase to another of a tapered crystal VO_2 beam grown on SiO_2 as shown in figure S6. Fig. S6a shows the topography of the taper, s-SNOM second harmonic optical amplitude images recorded at several temperatures are shown in figure S6b-d.

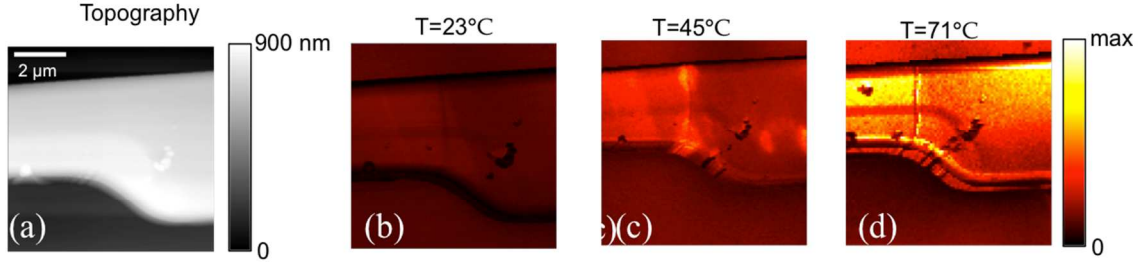


Fig. S6 Topography (a), s-SNOM second harmonic optical amplitude images (b-d) recorded at several temperatures at selected laser wavelength, $\lambda=10.7 \mu\text{m}$.

We selected to perform s-SNOM direct imaging of VO_2 beam at laser wavelength, $\lambda=10.7 \mu\text{m}$ because the dielectric constant of the insulating and metallic phases of VO_2 display significant differences at this wavelength that allow strong s-SNOM optical contrast. As discussed in the main text the thinner part of the taper generates brighter contrast than the wider side suggesting phase coexistence even at room temperature. As temperature is increased, inhomogeneous mixed phase dynamics across the taper is observed until the phase transition is more complete at higher T leading to a more uniformly bright near-field contrast. As described in literature, the stress due to the underlying substrate can affect phase nucleation in VO_2 . Hence, we use a freestanding suspended beam in Figure 4 in the main manuscript to illustrate a similar qualitative effect to demonstrate co-existence of the metallic and insulating phases at room temperature.

We have also performed s-SNOM on straight suspended VO_2 beams. Figure S7 shows the topography and near-field amplitude images of a straight suspended VO_2 beam. Unlike a tapered beam, which displays s-SNOM amplitude contrast at room temperature, the contrast in Fig. S7 evolves uniformly across the rod displaying an overall stronger signal, but no variation in contrast along the line profile in the metallic phase (71 C, Fig. S7c) compared to the insulating phase (26 C, Fig. S7b).

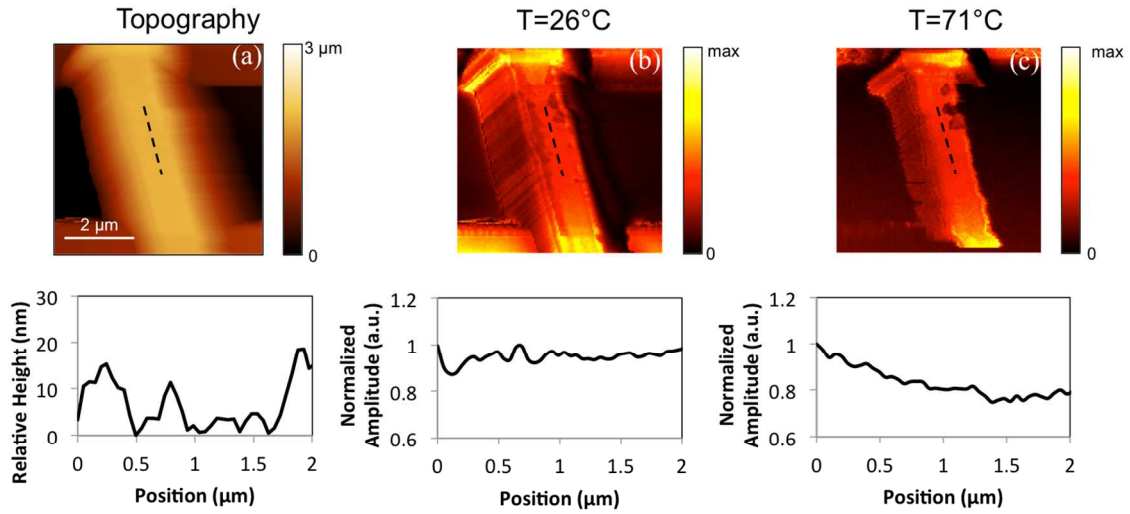


Fig. S7. Topography (a) and near-field amplitude images (b-c) of a straight suspended VO_2 beam. Unlike a tapered beam, which displays s-SNOM amplitude contrast at room temperature, the contrast in Fig S8 evolves uniformly across the rod displaying strong contrast in the metallic phase (71 C, Fig. S7c) compared to the insulating phase (26 C, Fig. S7b).

7. Auger Electron Spectra for Composition Analysis

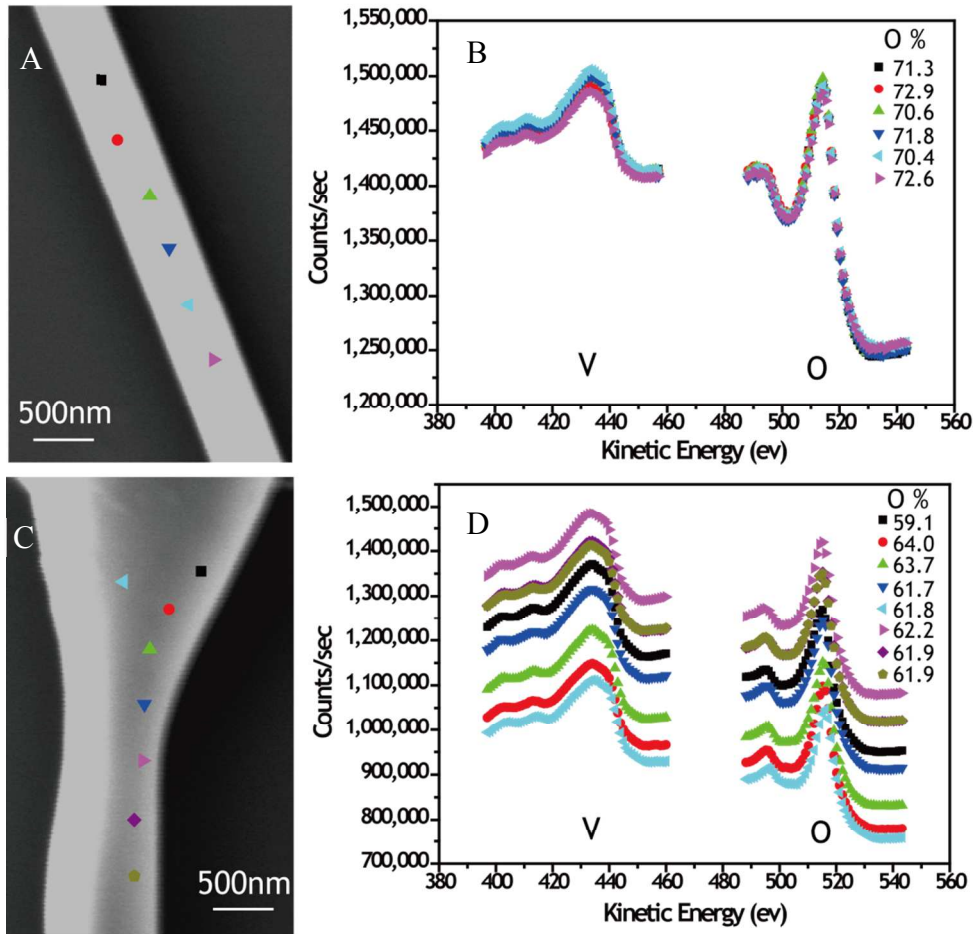


Fig. S8 A) Scanning Electron Microscopy (SEM) image of a uniform VO₂ beam, where the colored symbols represent locations used (~10nm resolution) for stoichiometric analysis. B) Auger Electron Spectra for the uniform VO₂ beam, with different colors representing the places labeled in A). C) Scanning Electron Microscopy (SEM) image of an asymmetric VO₂ beam, where the colored symbols represent places for stoichiometric analysis. D) Auger Electron Spectra for the asymmetric VO₂ beam, where the different colors represent the places labeled in C).

It is observed that the oxygen composition on the surface of the uniform beam is higher than 66.7% (as in VO₂). This oxygen-rich surface can be attributed to the general oxygen rich environment, as the beams are exposed to air during storage. It has been demonstrated in literature that exposing bulk VO₂ single crystals to an oxygen environment can produce surface oxidation tending towards V₂O₅ (71.4% oxygen)⁶. Such a study has not been performed on VO₂ beams grown using our techniques, but given the larger surface-to-volume ratio of such nano/micro scale beams, it is highly likely that the surface of the VO₂ beams in our study is oxygen-rich. Interestingly, it is observed that the oxygen composition on the surface of an asymmetric beam is lower than 66.7% (Fig. S8 (D)), despite the general oxygen rich environment. As discussed in

the main manuscript, the phase transition temperature is very sensitive to the stoichiometry of V_nO_{2n-1} . Hence, we expect these oxygen-deficient spots to remain in a metallic phase over a large range of temperatures (down to 135K for V_2O_3)^{7,8}.

8. The Impact of Thermal Contact Resistance

Since we measure the two-probe thermal conductance of the VO₂ beam, it is impossible to eliminate the effect of thermal contact resistance. The contribution of contact resistance between the nanobeam and the suspended membrane to the total measured thermal resistance can vary depending not only on the quality of the contact, but also the temperature drop across the nanobeam itself¹. Let's consider that the thermal conductivity of bulk VO₂ is ~4-6 W/m-K in the insulating phase at 300K⁹⁻¹¹. The typical cross-section of the beams is rectangular with the width, w and height, h around 500nm to 1.5 μ m. Consider for example beam IV (see Table 1) in the manuscript. The geometry of the beam is drawn below:

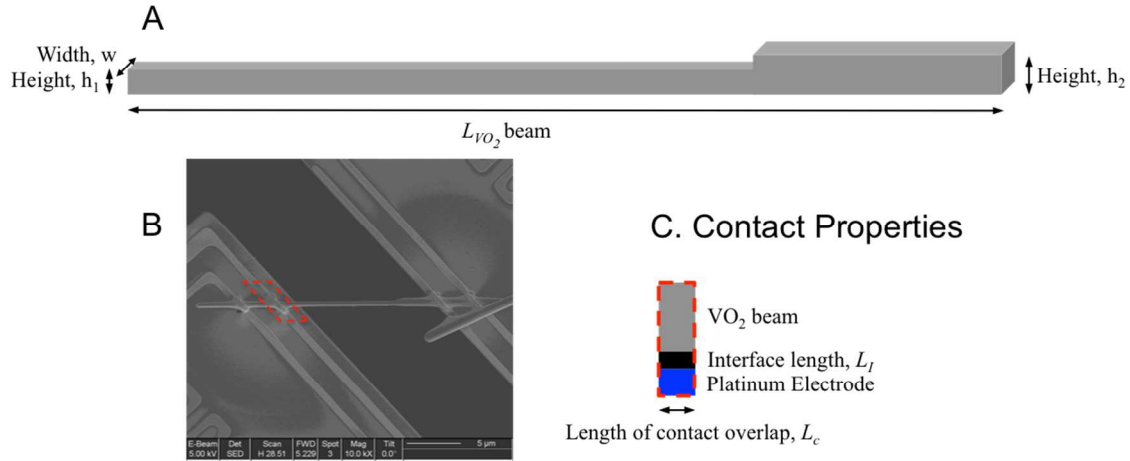


Fig. S9 A. A representation of the typical geometry of VO₂ beams used in this study. For beam IV (see Table 1 in main manuscript), $w = 270$ nm, $h_1 = 510$ nm, $h_2 = 820$ nm, $L_{VO_2} = 13.7$ μ m B. Top view Scanning Electron Micrograph of beam IV showing the asymmetrical geometry and Pt/C Focused Ion Beam Induced Deposits (FIBID) to improve thermal contact resistance and also provide electrical contact to the Platinum electrodes on the suspended membranes C. Cross-section diagram of each of four contacts between the VO₂ beam (grey) and the Platinum Electrode (blue) on the suspended membrane, with the interface (black). The length of the interface is defined as L_I , and the overlap between the VO₂ beam and the Platinum Electrode is defined as L_c .

Using an average cross-sectional area based on the dimensions shown above in Fig S9A, and approximating $k = 5 \text{ W/m-K}$ for the VO_2 beam, we expect the beam conductance to be 58.6 nW/K . The actual measured conductances G^+ and G^- are 56 and 48 nW/K respectively, which are agreeably close to the expected value. For other geometries of nanowires measured in this study, the range of measured thermal conductances is between 50 to 200 nW/K . This translates to the measured thermal resistance, $R_{\text{th}} = 1/G$ between the two pads of between 5 and $20 \text{ K/}\mu\text{W}$.

In order to estimate the effect of contact resistance, we follow the analysis in Yu et al.¹² and approximate the contacts between the beam and the membrane as rectangular fins. The thermal contact resistance R_c can be approximated as¹³:

$$R_c = \frac{1}{4} \cdot \frac{1}{\sqrt{hPkA_c} \tanh\left(\sqrt{\frac{hP}{kA_c}} L_c\right)} \quad (\text{SI } 3)$$

where h ($\text{W/m}^2\text{K}$) is the lateral heat transfer coefficient between the VO_2 beam and Platinum contact on the pads, $P=\text{width}$ is the effective perimeter of contacts performing as fins (the beam touches the membranes at the Platinum electrodes, each L_c in width as shown in Fig.S9C), k is the thermal conductivity of the VO_2 beam and $A_c = \text{width} \cdot \text{height}$ is the cross-sectional area of the beam. Let's approximate $h \approx k_l / L_l$ ¹², where k_l is the estimated thermal conductivity and L_l is the length of the ill-defined interface between the VO_2 beam and the Pt electrodes on the suspended membrane, as illustrated by Fig S9C in black. In order to determine the maximum possible thermal contact resistance, R_c , let us consider the scenario where the interface is sandwiched between the VO_2 beam and the Platinum electrode, as illustrated in Figure S9C.

The unknowns in Equation SI 3 are thus: k_I and L_I . Also, the area of contact changes for different widths of the beam, w .

- a) Interface conductivity, k_I : The worst scenario is all air contact, which is avoided by doing a tilted SEM and ensuring that the contact between the beam and Pt electrode is good. Once the FIBID based Pt/C composite is placed on the electrode, the area is observed with tilted SEM to be filled. Hence, the realistic lower limit is Pt/C composite with 30% Pt. This is an organometallic, with Pt particles joined by an organic substance¹⁴ and is known to resemble metal powders with 30% porosity (air gaps), who have a lower limit of thermal conductivity of $k_I=1$ W/m-K¹⁵. In the other extreme, the best-case scenario in the limit of perfect contact, is the Pt thermal conductivity itself, which is 20-30 W/m-K depending on the grain sizes for thin film Platinum.
- b) Length of the interface, L_I : The length of the contact can be approximated to span values from 1 nm to 100 nm as an extreme case.

Taking these length scales into considerations, Fig S10 shows the values of the thermal contact resistance (R_c) for different values of the unknown parameters:

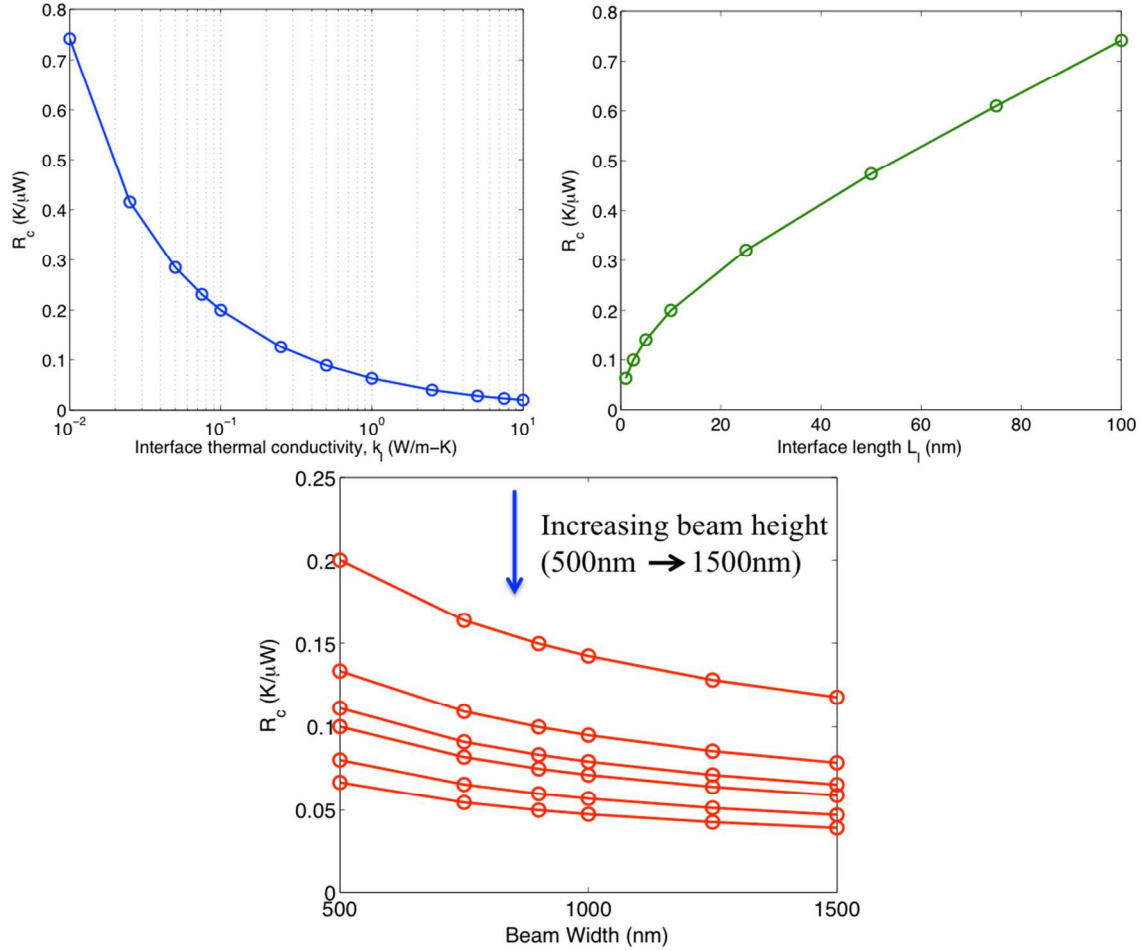


Fig. S10A. The thermal contact resistance, R_c as a function of the interface thermal conductivity, k_l approximating the contact area as a fin with adiabatic ends and a contact length of $1\mu\text{m}$. The maximum $R_c \sim 0.75 \text{ K}/\mu\text{W}$ is when $k_l = 0.01 \text{ W}/\text{m-K}$. For this graph, $L_I = 10 \text{ nm}$, $w = 500 \text{ nm}$ and $h = 500 \text{ nm}$. **B.** Predicted thermal contact resistance, R_c as a function of expected values of the interface length, L_I ranging from 1 to 100 nm where $k_l = 0.1 \text{ W}/\text{m-K}$, $w = 500 \text{ nm}$ and $h = 500 \text{ nm}$. **C.** Predicted thermal contact resistance, R_c as a function of beam widths and heights ranging from 500 nm to $1.5 \mu\text{m}$ when $k_l = 0.1 \text{ W}/\text{m-K}$ and $L_I = 10 \text{ nm}$.

In Fig. S10A, we have plotted R_c as a function of different k_l ranging from $0.01 \text{ W}/\text{m-K}$ to $10 \text{ W}/\text{m-K}$. As can be seen from Fig. S10A, R_c is expected to be $< 0.75 \text{ K}/\mu\text{W}$ for a large area of contact, which is at most 15% of our measured resistance. Note that we have used a beam width and height of 500 nm and $L_I = 10 \text{ nm}$. Fig. S10B shows the

effect that the interface length, L_I has on R_c . Even in the extreme case of $L_I = 100$ nm, assuming $k_I = 0.1$ W/m-K, we only get $R_c \sim 0.75$ K/ μ W. Finally, as expected, the contact resistance decreases as we increase the beam width upto 1.5 μ m, as the area of contact increases as illustrated in Fig. S10C. Here, we assume $k_I = 0.1$ W/m-K and $L_I = 10$ nm.

Another way of estimating the contact resistance is by considering the thermal interface resistance reported in literature for highly dissimilar materials. Even in this limit, the smallest thermal interface conductance between two solids is given by $G_c' \sim 10$ MW/m²-K¹⁶. Considering this value for the contact area in our system given by $w = 500$ nm, $L_c = 1$ μ m, we obtain

$$R_c = 2 \cdot \frac{1}{G_c' A} < \frac{2}{(10 \text{ MW m}^{-2} \text{ K}^{-1} \cdot 500 \text{ nm} \cdot 1 \mu\text{m})} = 0.4 \text{ K}/\mu\text{W}, \text{ which is at most}$$

8% of our measured thermal resistance.

Also note that this contact resistance only assumes direct contact between the VO₂ beam and the Platinum contacts via the Pt/C composite on the suspended pads. In practice, this is alleviated by the focused ion beam induced deposition (FIBID) of a Pt/C composite, which (1) increases the contact area between the VO₂ beam and the suspended membrane and (2) fills in any air gaps in the dry interface at the points of contact with the organometallic Pt/C substance. It has been shown previously that the total measured thermal resistance (including the contact) can be reduced by 10-15% by depositing this composite using the FIBID^{12,17-19}.

Further, we have used a non-tapered VO₂ beam whose geometry was carefully ascertained with cross-sectional SEM. The measured thermal conductance was 49.6 nW/K, $R_{th} = 20.2$ K/ μ W. The thermal conductivity matches that of bulk, $k \sim 5.5$ W/m-K at room temperature, which indicates that when heat flows from the suspended membranes

into the nanowire, most of the temperature drop occurs across the beam and the discontinuity in temperature at the contact is small. Based on the analysis above and Fig. SI 10A, $R_c < 0.75 \text{ K}/\mu\text{W}$, which is at most 2% of the measured resistance without considering the additional improvement in contact from the Focused Ion Beam Induced Deposition (FIBID) of Pt/C.

Next, we show below that the thermal contact resistance alone cannot explain the asymmetrical behavior of heat flow. Consider the case where the contact resistance has different temperature dependences at a particular gate temperature; this could result in rectification. Following the analysis of Dames, we can estimate an upper bound for thermal rectification due to contact resistance as shown in Figure 8(b) in the referenced manuscript, where the contacts are shown to dominate the thermal resistance across the two ends and the two contact ‘segments’ are labeled 1 and 2, respectively. Specifically, using Equation (24) of the referenced manuscript, the rectification can be described as:

$$\gamma = \frac{n_1 - n_2}{(\rho^{1/2} + \rho^{-1/2})^2} \Delta \quad (\text{SI } 4)$$

where γ is the rectification, n_1 and n_2 are the temperature exponents that defines the temperature-dependence of thermal conductivity near gate temperature T_G for each contact segment, ρ is the ratio R_2/R_1 where R_i is the thermal resistance of each segment and $\Delta = (T_h - T_s)/T_G$ is a normalized temperature with respect to the gate temperature. If the contacts are treated as thin heat conductors, then $(n_1 - n_2) \leq 6$. However, if the contacts are treated as a mismatch between the two materials at the contact, $(n_1 - n_2) \leq 3$ (see Reference ²⁰ for details). To maximize the rectification at a particular Δ , the

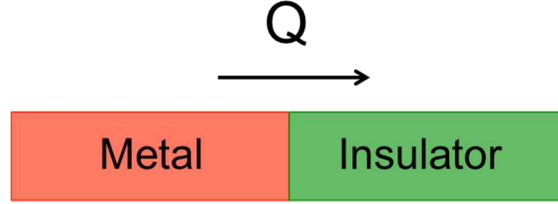
denominator needs to be minimized, which gives us $\rho = 1$. Then, for our experiments performed in the low-bias limit, where $(T_h - T_s) \leq 2K$ and $T_G \approx 300K$,

$$\gamma_{\max} \approx \frac{6}{4} \times \frac{2}{300} = 1\%.$$

In summary, first, the measured thermal conductances for all the VO₂ beams lie between 5 and 20 K/ μ W, with the maximum thermal contact resistance of 0.75 K/ μ W. This is expected to improve after Pt/C deposition using a FIB, which was also used to make electrical contact to the suspended VO₂ beam. The measured thermal conductivity (~ 5.5 W/m-K) of a uniform VO₂ beam indicates that the thermal contact resistance in our measurement is negligible since the measured value matches that of bulk. Secondly, even in the limiting case of thermal contact resistance dominating, for the low-bias experiment we have performed, maximum rectification in the system could atmost be 1%.

9. Estimation of Metal-Insulator Thermal Interface Resistance

If we consider electron-phonon inequilibrium at the Metal-Insulator interface, in the configuration illustrated below:



Here, the heat flows from the metal to the insulator. Using the two-temperature model as described in ²¹, the interface conductance, h_I can be defined as:

$$h_I = \frac{k_p \sqrt{\frac{G_{e-l}}{k_{hm}}}}{1 + \frac{k_p}{h_{pp}} \cdot \sqrt{\frac{G_{e-l}}{k_{hm}} - \frac{k_{hm}}{k_e}}} \quad (\text{SI } 5)$$

where k_p and k_e are the phononic and electronic thermal conductivities on the metallic side and k_{hm} is the harmonic mean given by: $k_{hm} = (1/k_p + 1/k_e)^{-1}$, h_{pp} is the phonon-phonon interface conductance, and G_{e-l} is the electron-phonon cooling rate. For a normal metal, $k_e \gg k_p$. However, for VO2 we need three cases, when the total thermal conductivity is estimated as $k_T = 10 \text{ Wm}^{-1}\text{K}^{-1}$.

(a) if Weidemann-Franz law is violated and $k_e=0$, then $k_p = 10 \text{ Wm}^{-1}\text{K}^{-1}$ and $k_{hm} = 0 \text{ Wm}^{-1}\text{K}^{-1}$.

(b) If Weidemann-Franz law is valid, and

$$k_e = L\sigma T = (2.44 \times 10^{-8}) \cdot (1 \times 10^6) \cdot (350) = 8.5 \text{ Wm}^{-1}\text{K}^{-1}. \text{ Then, } k_p = 1.5 \text{ Wm}^{-1}\text{K}^{-1} \text{ and } k_{hm} = 1.275 \text{ Wm}^{-1}\text{K}^{-1}.$$

(c) If there is equal contribution from the electrons and phonons to the total thermal conductivity, $k_e = k_p = 5 \text{ Wm}^{-1}\text{K}^{-1}$ and $k_{hm} = 2.5 \text{ Wm}^{-1}\text{K}^{-1}$.

In the insulating state, $G_{e-l} \sim (0.1-3)e^{16} \text{ Wm}^{-3}\text{K}^{-1}$ ²². Also, since the lattice mismatch between the metallic and insulating state is very small, we can assume that the phonon-

phonon interface resistance is very high, $h_{pp} \sim 100 \text{ MWm}^{-2}\text{K}^{-1}$. Since $h_I \propto h_{pp}$, this assumption will give us a conservative over-estimate of the interface conductance. Then, using Equation (SI 5) and substituting values for all three cases, we find that h_I ranges from ~ 33 to $92 \text{ MWm}^{-2}\text{K}^{-1}$.

Now, consider our measured thermal conductance of the VO_2 beam to be $G_T = 100 \text{ nWK}^{-1}$, and hence total measured thermal resistance including the metal-insulator interface is given by $R_T = 1/G_T = 1e7 \text{ KW}^{-1}$. Since the total resistance is a series resistance of the metallic and insulating elements and the metal-insulator interface, if we assume that the observed thermal rectification comes purely from the metal-insulator interface, then for a rectification of 25%, the interface thermal resistance has to be given by: $R_I = 0.25 \cdot R_T = 2.5e6 \text{ KW}^{-1}$.

If we take this to be the measured interface resistance, then we can estimate how much area we need given the thermal interface conductance, h_I calculated above. Then, $A_I = 1/h_I R_I$ gives an estimated effective-interface area $A_I \approx 4350 - 12120 \text{ nm}^2$. If we approximate this interface to be a square cross-section, then the lateral dimensions would be $(\sim 66 \times 66) \text{ nm}^2$ up to $(\sim 110 \times 110) \text{ nm}^2$. Of course, this estimate of the interface area depends upon the total measured thermal conductance and the rectification magnitude.

10. Error Analysis for Thermal Conductance Measurements

In the thermal measurement scheme, the conductance of the beam is determined by ramping up the temperature in a stepwise (50 steps) fashion by passing a DC current (0-8 μA) through the PRT on the heating membrane. The rise in temperature on either side is monitored by measuring the resistances, R_s and R_h on both platforms, as seen in Fig S11 below. For a Platinum Resistance Thermometer (PRT) in the temperature range of our measurement (50K-300K), the resistance changes linearly with temperature:

$$\Delta R_s = (R_s - R_{s,G}) \propto (T_s - T_G) = \Delta T_s \text{ and } \Delta R_h = (R_h - R_{h,G}) \propto (T_h - T_G) = \Delta T_h$$

Since the rise in temperature is proportional to the supplied power through I_h ,

$$\Delta T_h \propto I_h^2 R_{h,G} \text{ and } \Delta T_s \propto I_h^2 R_{h,G}.$$

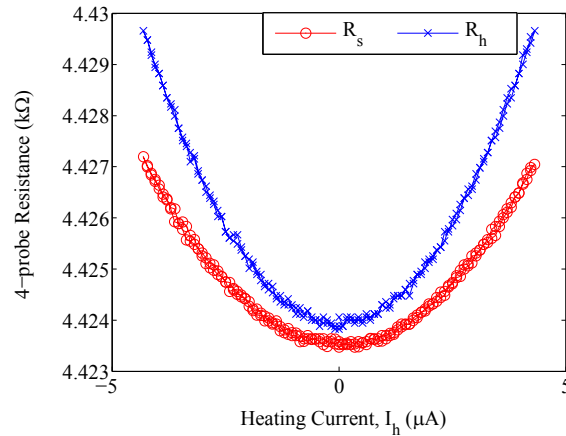


Fig. S11 R_s and R_h as a function of the heating current, I_h . Resistance is proportional to temperature, which in turn is proportional to the power supplied by joule heating. Thus, the resistance has a quadratic dependence on I_h

Following the analysis of Equation (SI 2), the heat flow in the VO_2 beam can be

estimated as: $Q = \gamma \cdot \frac{I_h^2 R_h}{(\Delta T_h + \Delta T_s)} \cdot \Delta T_s$, where γ is a non-dimensional ratio of the resistance

of the PRT and the resistance of the suspended legs. γ is a constant at all temperatures.

The beam conductance can then be determined using the relation $G = Q / (\Delta T_h - \Delta T_s)$. Then,

error propagation rules determine that:

$$\left(\frac{\delta Q}{Q}\right)^2 = 2 \cdot \left(\frac{\delta I_h}{I_h}\right)^2 + \left(\frac{\delta R_h}{R_h}\right)^2 + \left(\frac{\delta(\Delta T_s)}{\Delta T_s}\right)^2 + \left(\frac{\delta(\Delta T_h + \Delta T_s)}{\Delta T_h + \Delta T_s}\right)^2 \quad (\text{SI } 5)$$

$$\text{and, } \left(\frac{\delta G}{G}\right)^2 = \left(\frac{\delta Q}{Q}\right)^2 + \left(\frac{\delta(\Delta T_h - \Delta T_s)}{\Delta T_h - \Delta T_s}\right)^2 \quad (\text{SI } 6)$$

Hence, the following error terms need to be determined:

$$(1) \frac{\delta R_h}{R_h}, (2) \frac{\delta(\Delta T_s)}{\Delta T_s}, (3) \frac{\delta(\Delta T_h + \Delta T_s)}{\Delta T_h + \Delta T_s} \text{ and } (4) \frac{\delta(\Delta T_h - \Delta T_s)}{\Delta T_h - \Delta T_s}$$

The linear dependence of the PRT resistance with respect to temperature allows us to define ΔT_s and ΔT_h . One cycle of measurement constitutes gathering this raw data at 5 different local temperature points around T_G . Consider the partial derivative

$$\frac{\partial R_{h/s}}{\partial T_{h/s}} \approx \frac{\Delta R_{h/s}}{\Delta T_{h/s}} \text{ at } T_G = 300\text{K. Then, we measure the resistances } R_{s,G} \text{ and } R_{h,G} \text{ at}$$

295K, 298K, 300K, 302K and 305K. The plot of resistance as a function of gate temperature is typically a line as below:

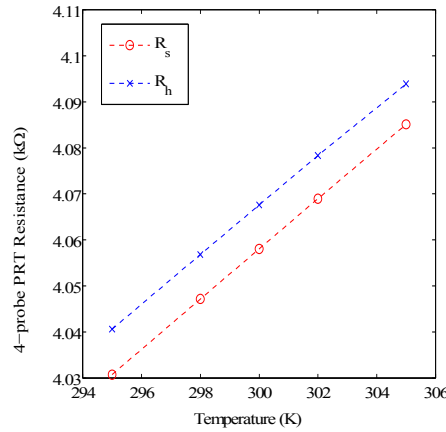


Fig. S12 Measured R_s and R_h around $T_G=300\text{K}$ used for calibration of TCR.

If we define $\alpha_s \equiv \frac{dR_s}{dT_G} \sim \frac{\Delta R_s}{\Delta T_G}$ and $\alpha_h \equiv \frac{dR_h}{dT_G} \sim \frac{\Delta R_h}{\Delta T_G}$ then these slopes can be determined to very high accuracy. In general, $\frac{\delta\alpha_s}{\alpha_s}$ and $\frac{\delta\alpha_h}{\alpha_h} \leq 1.75 \times 10^{-2}$ when $R^2 > 0.9999$ for the least squares fitting shown in Fig. S12 above. To understand where this error comes from, consider the following error propagation (where $i = h$ or s):

$$\left(\frac{\delta\alpha_i}{\alpha_i}\right)^2 = \left(\frac{\delta(\Delta R_i)}{\Delta R_i}\right)^2 + \left(\frac{\delta(\Delta T_i)}{\Delta T_i}\right)^2$$

Following the analysis of Shi ², we have verified that $\frac{\delta R_i}{R_i} = \sqrt{\left(\frac{\delta v_{out}}{v_{out}}\right)^2 + \left(\frac{\delta i_{ac}}{i_{ac}}\right)^2} \approx 5 \times 10^{-5}$

from the AC measurements of the 4-probe resistance using a lock-in amplifier on both the heating and sensing sides. We haven't described the detailed error contributions for this term, but these are similar to those calculated in Shi ¹ and Li ² and as is seen later in this analysis, two orders of magnitude smaller in comparison to other sources of error in the measurement.

To determine the slope α_i , we use a temperature excursion of $\Delta T = 10K$. Then,

$\delta(\Delta T_i) = \sqrt{2} \cdot \delta T_i \approx \sqrt{2} \cdot 40mK = 57mK$. Hence, $\frac{\delta(\Delta T_i)}{\Delta T_i} \approx \frac{57mK}{10K} \approx 5.7 \times 10^{-3}$. Therefore, we

should expect $\left(\frac{\delta\alpha_i}{\alpha_i}\right) \approx 6 \times 10^{-3}$ at most from direct measurement of the 4-probe resistance

and the cryostat temperature. However, this analysis doesn't account for temperature fluctuations of the cryostat $\sim 30-40mK$ (at room temperature) which are unavoidable. We wait for up to 60 minutes at each gate temperature for the cryostat head temperature to stabilize. Hence, the maximum standard deviation of the estimated slope for either R_h or R_s is given by σ_α (obtained from the the least-squares linear fit to the Resistance, R_i vs

Temperature, T_i curve) where i represents either the heating or the sensing side. The equation that determines this value is:

$$\sigma_{\alpha}^2 = \sigma_R^2 \bullet \frac{n}{n \sum_i T_i^2 - \left(\sum_i T_i \right)^2}$$

where σ_R is the standard error for the Resistance estimate (either heating or sensing side)

and n is the number of points taken (in this case, 5). σ_R is given by:

$$\sigma_R^2 = \frac{1}{n-2} \sum_i (R_i - \alpha T_i)^2$$

Then, in order to estimate the 95% confidence interval of the slope (considering two-tailed uniform distribution), we obtain a t-value of 3.182 for 3 ($n-2$) degrees of freedom.

Thus, the maximum possible error in the slope is:

$$\delta\alpha_i = t_{(n-2)} \bullet \sigma_{\alpha}$$

which in terms of percentage can be written as (for beam I):

$$\frac{\delta\alpha_i}{\alpha_i} \leq 0.76\%$$

Now, the error in ΔT_s and ΔT_h can be determined from the relation:

$$\frac{\delta(\Delta T_i)}{\Delta T_i} = \sqrt{\left(\frac{\delta(\Delta R_i)}{R_i} \right)^2 + \left(\frac{\delta\alpha_i}{\alpha_i} \right)^2} \approx \sqrt{(5 \times 10^{-5})^2 + (0.76 \times 10^{-2})^2} \approx 0.76 \times 10^{-2} = 0.76\%$$

Or as a general expression, $\frac{\delta(\Delta T_i)}{\Delta T_i} \approx \frac{\delta\alpha_i}{\alpha_i}$ where i stands for h (heating) or s (sensing).

Let us define $e_{\alpha_i} \equiv \frac{\delta\alpha_i}{\alpha_i}$.

Then, $\frac{\delta(\Delta T_i)}{\Delta T_i} \approx e_{\alpha_i}$

Now,

$$\frac{\delta(\Delta T_h + \Delta T_s)}{\Delta T_h + \Delta T_s} = \frac{\sqrt{[\delta(\Delta T_h)]^2 + [\delta(\Delta T_s)]^2}}{\Delta T_h + \Delta T_s} = \frac{\sqrt{(e_{\alpha_h} \cdot \Delta T_h)^2 + (e_{\alpha_s} \cdot \Delta T_s)^2}}{\Delta T_h + \Delta T_s}$$

Hence, from Equation (SI 5), neglecting the small error contributions due to terms $\frac{\delta I_h}{I_h}$

and $\frac{\delta R_h}{R_h}$, we can rewrite this equation as:

$$\left(\frac{\delta Q}{Q}\right)^2 \approx \left(\frac{\delta(\Delta T_s)}{\Delta T_s}\right)^2 + \left(\frac{\delta(\Delta T_h + \Delta T_s)}{\Delta T_h + \Delta T_s}\right)^2 \quad (\text{SI 5a})$$

which can be simplified with some simple algebra to determine the absolute error in the measured heat flux, δQ :

$$\delta Q = Q \cdot \sqrt{(e_{\alpha_s})^2 + \frac{(e_{\alpha_h} \cdot \Delta T_h)^2 + (e_{\alpha_s} \cdot \Delta T_s)^2}{(\Delta T_h + \Delta T_s)^2}} \quad (\text{SI 7})$$

We can thus estimate the error in Q(heat flux) for each ΔT (for beam I) to be:

$$\frac{\delta Q}{Q} = \sqrt{2 \cdot (4.2 \times 10^{-5})^2 + (5 \times 10^{-5})^2 + (0.76 \times 10^{-2})^2 + (1.2 \times 10^{-2})^2} \approx 1.4\%$$

Then, the error in conductance, G if defined as $Q/\Delta T$ is given by Equation (SI 6):

$$\frac{\delta G}{G} = \sqrt{(1.4 \times 10^{-2})^2 + (1.66 \times 10^{-2})^2} \approx 2.2\%$$

However, this is the error obtained for a single data-point for the case $G \equiv \frac{Q}{\Delta T}$. In

practice, we obtain 200 such points during each measurement cycle as shown in Fig. S12

above. Further, we repeat each measurement cycle 2-3 times to ensure repeatability of

the data. Hence, a more accurate estimation of the beam conductance is given by the slope of the Q vs ΔT curve as the current, I_h , is ramped up. The difference is illustrated in the cartoon below:

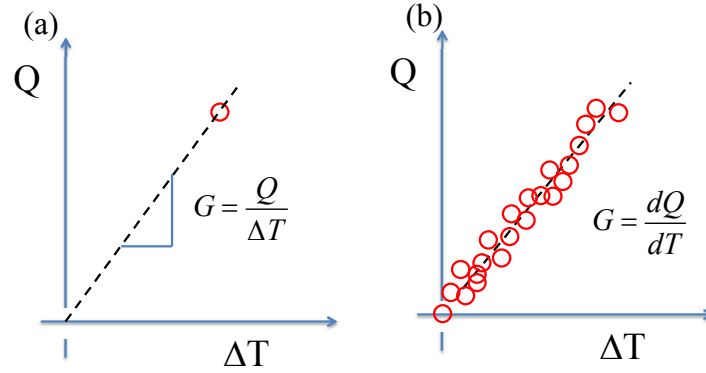


Fig. S13 Illustration of the difference in definition of the conductance either by considering (a) a single data-point with a large enough ΔT , or (b) taking the local slope of the heat flux for a variety of temperature gradients across the suspended beam.

To revisit the error bars in the case of Fig. S13(b), a similar analysis as described above can be performed. Since the slope of the Q vs ΔT curve (forcing the intercept to zero), gives the conductance, G , the standard error for the heat flux estimate as well as the error in conductance can be ascertained. As an example, data is reproduced below for beam I (see Table 1) in the manuscript:

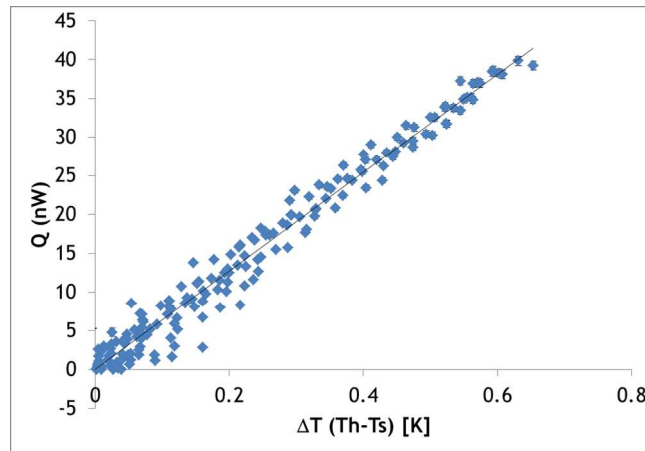


Fig S14 Heat flow through the tapered VO_2 beam I, Q in nW as a function of the temperature difference across the beam, ΔT in K at $T_G = 300\text{K}$.

Most importantly here, the error in heat flux is experimentally determined and can be called the pure error of each data point.

Hence, the conductance can be determined by doing a linear least-squared fit to the data.

In our case however, weightage from the errors at small ΔT is overwhelming. Also, the variability in data for small ΔT is larger, thus the variance in the error is larger. As an example, consider the following residual plot in Fig S15(a), where the residual is defined as:

$$\varepsilon_i = Q_i - G_{fit} \Delta T$$

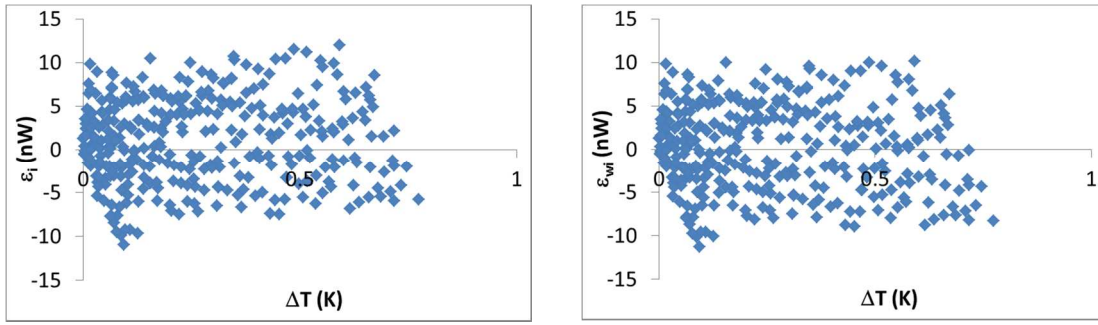


Fig S15(a) Residual plot for linear least-squared fit and (b) weighted linear least-squared fit, with a weight given by $w_i = 1/\delta Q^2$

Taking advantage of the large number of data points we gather at every global temperature, T_G we use the weighted least squares method to estimate the slope of the Q vs ΔT data. Similar to a simple linear least-squares regression, this will minimize the weighted residuals $s_w(G') = \sum_i w_i (Q_i - G' \Delta T_i)^2$, where $w_i = 1/\delta Q^2$

(see Fig S15b). This provides two advantages:

- (1) it accounts for the non-equal error variance in the small ΔT case, and

(2) it incorporates the pure error, δQ in Q measurement at every ΔT in to the linear fit and hence accounts for actual experimental uncertainty.

It has been proven that such a weighted least-squares estimate is the best linear unbiased estimator (BLUE) when the weight is equal to the reciprocal of the measurement variance. Once the weighted least-squares fitting is completed, we can then estimate the error in conductance by considering the two-tailed 95% confidence interval with a $t_{(n-2)}$ value of 1.96 for $n > 100$. Thus, the error in conductance is given by $\delta G = \sigma_G \cdot (1.96)$.

In summary, for all beams measured, repeated measurements (2-3 times at each gate temperature) account for the error in Temperature Coefficient of Resistivity (TCR) of the Platinum Resistance Thermometers (PRTs), thus reducing the error in measured α_h and α_s . Secondly, slowly ramping up the heating current to get ~50-100 data points per temperature excursion allows for accurate estimation of the beam thermal conductance within 1% (depending on the cryostat temperature oscillations during measurement for each global gate temperature).

Finally, for our definition of error in rectification given by $R = \frac{G_+ - G_-}{G_-}$, we obtain for

Beam I:

$$\frac{\delta R}{R} = \sqrt{\left(\frac{dG_+}{G_+}\right)^2 + \left(\frac{dG_-}{G_-}\right)^2} = \sqrt{\left(\frac{\delta G_+}{G_-}\right)^2 + \left(\frac{G_+}{G_-^2} \delta G_-\right)^2} \approx 1.3\% \quad (\text{SI } 8)$$

where $G_+ \pm \delta G_+ = 80.1 \pm 0.6 \text{ nW/K}$ and $G_- \pm \delta G_- = 62.2 \pm 0.4 \text{ nW/K}$. A similar methodology is adopted to determine the error in thermal rectification for each of the VO₂ beams measured in the manuscript.

References

- (1) Shi, L.; Li, D.; Yu, C.; Jang, W.; Kim, D.; Yao, Z.; Kim, P.; Majumdar, A. *J. Heat Transfer* **2003**, *125*, 881-888.
- (2) Li, D. Thermal Transport in Individual Nanowires and Nanotubes, UC Berkeley, 2002.
- (3) Keilmann, F.; Hillenbrand, R. *Philos. Trans. R. Soc. London A* **2004**, *362*, 787–805.
- (4) Qazilbash, M. M.; Brehm, M.; Chae, B.-G.; Ho, P.-C.; Andreev, G. O.; Kim, B.-J.; Yun, S. J.; Balatsky, a V; Maple, M. B.; Keilmann, F.; Kim, H.-T.; Basov, D. N. *Science* **2007**, *318*, 1750–1753.
- (5) Ocelic, N.; Huber, A.; Hillenbrand, R. *Appl. Phys. Lett.* **2006**, *89*, 1–3.
- (6) Parker, J. *Phys. Rev. B* **1990**, *42*, 3164–3166.
- (7) Kachi, S.; Kosuge, K.; Okinaka, H. *J. Solid State Chem.* **1973**, *6*, 258–270.
- (8) Wells, A. F. *Structural Inorganic Chemistry*; Oxford Classic Texts in the Physical Sciences; OUP Oxford, 2012.
- (9) Andreev, V. N.; Chudnovskii, F. A.; Petrov, A. V; Terukov, E. I. *Phys. Status Solidi* **1978**, *48*, K153–156.
- (10) Berglund, C.; Guggenheim, H. *Phys. Rev.* **1969**, *185*, 1022–1033.
- (11) Oh, D.-W.; Ko, C.; Ramanathan, S.; Cahill, D. G. *Appl. Phys. Lett.* **2010**, *96*, 151906.
- (12) Yu, C.; Saha, S.; Zhou, J.; Shi, L.; Cassell, A. M.; Cruden, B. A.; Ngo, Q.; Li, J. *J. Heat Transfer* **2006**, *128*, 234-239.
- (13) Incropera, F. P.; DeWitt, D. P. *Introduction to Heat Transfer*; Wiley, 2001.
- (14) Utke, I.; Hoffmann, P.; Melngailis, J. *J. Vac. Sci. Technol. B Microelectron. Nanom. Struct.* **2008**, *26*, 1197-1276.
- (15) Hadley, G. R. *Int. J. Heat Mass Transf.* **1986**, *29*, 909–920.
- (16) Lyeo, H.-K.; Cahill, D. *Phys. Rev. B* **2006**, *73*, 1–6.

- (17) Mavrokefalos, A.; Pettes, M. T.; Zhou, F.; Shi, L. *Rev. Sci. Instrum.* **2007**, *78*, 034901.
- (18) Hochbaum, A. I.; Chen, R.; Delgado, R. D.; Liang, W.; Garnett, E. C.; Najarian, M.; Majumdar, A.; Yang, P. *Nature* **2008**, *451*, 163–167.
- (19) Li, D.; Wu, Y.; Kim, P.; Shi, L.; Yang, P.; Majumdar, A. *Appl. Phys. Lett.* **2003**, *83*, 2934-2936.
- (20) Dames, C. *J. Heat Transfer* **2009**, *131*, 061301.
- (21) Majumdar, A.; Reddy, P. *Appl. Phys. Lett.* **2004**, *84*, 4768-4770.
- (22) Tao, Z.; Han, T.-R. T.; Ruan, C.-Y. *Phys. Rev. B* **2013**, *87*, 235124.